On Water Transfer and Hydraulic Connection Layer During the Convective Drying of Rigid Porous Material

**N. Prime · Z. Housni · L. Fraikin · A. Léonard ·
R. Charlier · S. Levasseur**

Abstract The convective drying of a natural porous material, limestone, is investigated in this study, with both experimental and numerical approaches. The first experimental campaign, which focuses on the influence of samples' slenderness, suggests the presence of a hydraulic connection layer between the porous water and the external environment, in spite of the very fine pore structure of the material. This hydraulic transfer enables the fast water evaporation at the beginning of the drying test, when external conditions drive the kinetics. Furthermore, the results show that this layer does not exceed 30 mm deep from the external surface, given the drying conditions of the test. A second experimental campaign aims to analyse, by mean of an X-ray tomography tool, the internal water content during the drying. It confirms that water transfer takes place within the limestone in two distinct stages. The first stage being faster than the second one with a homogeneous desaturation along the sample, it is consistent with the hypothesis of the hydraulic connection layer. Finally, the finite element modelling makes possible to identify the main mechanisms of water transfer, namely liquid convection and vapour diffusion.

List of symbols

$\dot{\mathbf{m}}_{\mathbf{l}}$	Hydraulic mass flux vector (kg/s/m^2)
$\dot{\mathbf{m}}_{\mathbf{v}}$	Water vapour mass flux vector (kg/s/m^2)
$\mathbf{g}$	Gravity acceleration vector (m/s^2)
$\dot{\boldsymbol{q}}$	Heat flux vector (W/m^2/°K)
∇	Gradient operator
ΔH_{cap}	Head difference due to capillary effects (m)

N. Prime (✉) · Z. Housni · L. Fraikin · A. Léonard · R. Charlier · S. Levasseur
Université de Liège, Chemin des Chevreuils 1, 4000 Liège, Belgium
e-mail: noemie.prime@gmail.com

ΔH_v	Head difference due to viscous effects (m)
δ	Limit layer width (m)
$\dot{m}$	Water mass flux (kg/m^2/s)
$\dot{m}_{cst}$	Constant mass flux during the CRP (kg/m^2/s)
$\dot{q}$	Heat flux (W/m^2)
$\dot{v}$	Volumetric flux of liquid water through the fine tube of the capillary model (m/s)
$\dot{v}_o$	Global volumetric flux of evaporation for the capillary model (m/s)
η	Dynamic viscosity of water (Pa.s)
Γ	Thermal conductivity (W/m/°K)
κ	Intrinsic permeability (m^2)
μ	Attenuation coefficient to X-rays (m^{-1})
ϕ	Porosity (–)
ρ_s	Solid density (kg/m^3)
ρ_v	Vapour density (kg/m^3)
ρ_w	Liquid water density (kg/m^3)
$\rho_{v,air}$	Ambient vapour density (kg/m^3)
$\rho_{v,sat}$	Saturated vapour density (kg/m^3)
$\rho_{v,surf}$	Vapour density on the wet drying surface (kg/m^3)
σ	Surface tension (N/m)
τ	Tortuosity (–)
a, b	Constants determined by Vinegar and Wellington (1987) for the computation of attenuation coefficients
$c_{p,s}$	Specific heat of solid phase (J/kg/°K)
$c_{p,v}$	Specific heat of water vapour (J/kg/°K)
$c_{p,w}$	Specific heat of liquid water (J/kg/°K)
D	Diffusion coefficient of vapour into dry air (m^2/s)
E	Energy of X-rays (keV)
g	Gravity acceleration (m/s^2)
H	Sample's height (m)
h	Heat transfer coefficient (W/m^2/°K)
h_m	Mass transfer coefficient (m/s)
K	Hydraulic conductivity (m/s)
$k_{r,w}$	Relative permeability coefficient (–)
L	Latent heat (J/kg)
l	Characteristic length (m)
M	Mass (g)
M_v	Molar mass of water (kg/mol)
m	Van Genuchten fitting parameter (–)
n	Van Genuchten fitting parameter (–)
p_a	Air entry pressure (Pa)
p_c	Capillary pressure (Pa)
p_g	Gaz pressure (Pa)
p_w	Liquid water pressure (Pa)
p_{atm}	Atmospheric pressure (Pa)
$p_{v,air}$	Ambient vapour pressure (Pa)
$p_{v,sat}$	Saturated vapour pressure (Pa)
R	Universal gaz constant (J/mol/kg)
r_1, r_2	Tubes' radii of the capillary model (m)

RH	Relative humidity (–)
S	Sample's drying area (m^2)
Sr	Water saturation degree (–)
Sr_{res}	Residual saturation degree (–)
T	Temperature (°K)
t	Time (s)
T_0	Initial temperature of the sample (°K)
T_h	Wet bulb temperature (°K)
T_{air}	Ambient temperature (°K)
T_{surf}	Temperature on the wet drying surface(°K)
V	Sample's volume (m^3)
W	Water content (kg/kg)
W_c	Critical water content (kg/kg)
Z	Atomic number (–)

1 Introduction

### 1.1 Diversity of Studied Materials Under Drying Conditions

Drying plays a major part in many industrial sectors as a way to conserve the matter, to reduce the volume of bulky materials, or to finalize the manufacture of a product after a processing under wet conditions. This is why drying investigations concern so many materials, as for instance food products (Léonard et al. 2008; May and Perré 2002), paper (Sherwood 1930), sludges (Léonard et al. 2005), etc.

But drying also occurs under natural conditions and is sometimes damageable. For instance, it is responsible of building stone alteration for a high number of drying-imbition cycles. It can also cause a loss of sealing properties of host rocks dedicated to nuclear waste storage once the underground cavities are excavated. Consequently, a large number of soils and rocks are also studied under drying conditions: kaolin clay (Ketelaars et al. 1995), sandstone (Rousset-Tournier et al. 2003), clayey formations (Musielak and Banaszak 2007; Cariou et al. 2012) etc.

To better understand the physics of drying, rather than improve industrial processes, simplified matters are also experimentally studied. For example, Shaw (1987) experimented the drying of silica bead packings and assimilated it to the flow of two immiscible fluids, air and water, classically modelled by invasion percolation (for example for oil recovery from a reservoir with water injection). Laurindo and Prat (1998) showed that during the drying of two dimensional square porous networks, an important part of water is transported under thin corner flows or film flows. Lastly, Faure and Coussot (2010) demonstrated that for a model soil made by a glass bead network filled with kaolin or bentonite suspension, the drying kinetics is governed by the pasty filling material.

1.2 Water Transfer During Drying

Even if a wide variety of drying processes is used (convective drying under air flow, conductive drying by contact with a heat source, solar drying, etc.), some general features of drying kinetics are well established. Notably, two phases are typically distinguished in the drying curves, both in the mass loss during time and in the evaporation flux evolution along the water content (the so-called Krischer's curve). During a first phase, called constant rate period
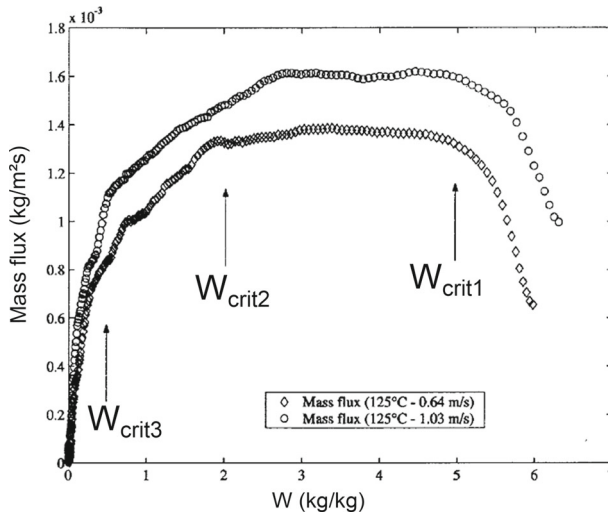
Fig. 1 Krischer's curve (showing the flux evolution along the water content W) obtained for the convective drying of a wastewater sludge (Léonard et al. 2002)

(CRP), the evaporation rate (that is to say the water mass flow divided by the evaporation surface) is constant. During the second, the falling rate period (FRP), this flux progressively decreases before vanishing. This phasing, described from decades can be clearly observed in the Krischer's curve, as for example in Fig. 1 for the convective drying of a wastewater sludge. In this figure appear: a preheating period beyond W_{crit1}, the CRP between W_{crit1} and W_{crit2} and the FRP below W_{crit2}.

It is commonly admitted that the CRP is characterized by a global evaporation rate that is lower than the ability of the material to supply water up to the sample surface. In consequence, only ambient conditions (temperature, hygrometry, etc.) control the global drying rate. This can be highlighted by varying these conditions as done for instance by Léonard et al. (2005). On the contrary, FRP is interpreted as a period during which the external evaporation demand is higher than the ability of the water to displace up to the material surface. In such phase, the global drying rate is thus governed by the internal structure of the material, rather than the ambient conditions, and depends on the permeability of the material, its tortuosity, etc. Consequently, Krischer's curve is known to vary a lot with the nature of the material, and notably it depends on whether the material is hygroscopic or not, that is to say if a part of the water is bounded to the solid skeleton or if it is all capillary or free water. Examples of different kinds of Krischer's curves are presented and compared in Van Brakel (1980).

To better interpret the transition between the CRP and the FRP, two hypothesis are classically proposed, the 'Wetted surface model' and the 'Receding Front model'. They are exposed for instance in Keey (1978). According to the 'Wetted Surface model', the first decrease of the flux is due to the apparition of dry zones in the external surface which limits the water transfers. This critical moisture of the surface is considered to correspond to a critical moisture content of the whole sample, denoted W_c. On the other hand, according to the 'Receding Front model', the end of the CRP is due to the loss of all the non-bounded water at the external surface, which induces a receding of the drying front inside the sample.

However, none of these models, taken independently, can explain the kinetics of drying tests on natural matter, because they result from complex and simultaneous modes of water

transfer (explained by diffusion, advection, capillary effect, gravity, etc.) and also because they vary a lot with the material considered. Besides, details of these two hypothesis can be questioned. First of all, a convective drying test performed on a sintered packing of glass beads (Van Brakel 1980) shows that, even during the CRP, the surface is significantly dried. Secondly, it seems unlikely that a value of W_c characterizes a given material without influence of the geometric proportions. Finally, the CRP is not even obtained for a great number of common materials such as apple (May and Perré 2002), silt (Gerard et al. 2010), etc. Although this is likely due to high internal limitations to the water transfer, it is not yet clearly understood.

More specifically, some investigations are currently converging to explain the transition from a high to a reduced evaporation rate (from the CRP to the FRP) by a transition from a hydraulic water transfer up to the surface toward a water vapour transfer. The earliest work that pointed out this effect, seems to have been led by Shaw (1987), who experimentally showed that the evaporation flux from the top of a cell filled with packed silica beads was higher than in an empty cell, where the water level decreases under the surface. This results were attributed to the counterflow along particle contacts which maintains a hydraulic flow up to the surface of the cell. This hypothesis has been later refined, notably by the experimental work done by Laurindo and Prat (1998) who proved the importance of corner and film flows during the first stage of drying for a 2D pore-network model. This theory has been then numerically demonstrated by Yiotis et al. (2005), who managed to reduce the discrepancy between experimental results and numerical predictions by considering film flows at the gas-water interface (also using a 2D square network model). Finally, the experimental and theoretical work of Lehmann et al. (2008) on sand has to be mentioned as it raised the notion of hydraulic connection layer between the surface of the sample and an internal drying front, and it proposed a relation between the width of this layer and the micro-structure of the material. Shokri et al. (2009) went more into details in describing the drying of sand by experimentally identifying a second physical limit inside the material, corresponding to the frontier between the hydraulic connection zone and the dry zone.

1.3 Modelling Drying Kinetics

From Sherwood (1929) works, drying models have been led during a long time by considering diffusion as the only mechanism for describing the whole water transfer. Ceaglske and Hougen (1937) first pointed that the Fick's law was not sufficient to describe drying, and that gravity, capillary effects, external pressure were to be taken into account as well. They proposed then to enhance the diffusion theory by considering diffusion coefficients which were function of the water content. Many authors followed this idea, up to quite recently with some studies in which apparent diffusion coefficients were experimentally determined through the water content analysed in the studied samples (Pel et al. 1996; McDonald et al. 1996). Philip and De Vries (1957) were among the first ones who developed a model which distinguished the liquid and the vapour transfer. Their approach is still based on diffusion but it takes into account the gravity effect for the liquid water transport. In the same period, Krischer (1956) presented the theory of a transfer of water that would be driven both by vapour flow, with Fick's law, and capillary flow, this time using Darcy's law. Developing this concept of a multi-mechanism transfer, Whitaker (1977) described, within a volume averaging framework, the drying kinetics as the result of liquid flow—by capillary forces-, vapour flow—by convection and diffusion forces- and heat flow—with convection and conduction forces. Up to now, this model is one of the most complete and can be solved numerically by various

methods as Finite Element Method, Finite Difference Method, Control Volume Method, etc.

1.4 Aim of the Article

The aim of this article is to extend all the theories, above mentioned, about the water transfers during drying for a rigid natural geomaterial. In particular the following questions can be raised: What does explain the first decrease of the evaporation flux? Is it linked to a critical water content of the whole material? Or can a hydraulic connection layer also be highlighted for a natural material, with a 3D geometry, a heterogeneous pore size distribution and a non-square porous network? Finally, can a coupled thermo-hydraulical Finite Element model capture the principal features of the kinetics with a convection law for the fluid and a diffusion law for the gaz?

To answer these points we consider in this study a natural porous material—the limestone-which does not undergo shrinkage nor cracking during drying. The first part of the paper is dedicated to experimental investigations (Sect. 2), focusing, on one hand, on the influence of the Volume/Surface ratio of the dried samples and, on the other hand, on the evolution of the saturation profile inside the material, by mean of a X-ray tomographic tool. In a second part, the drying tests are simulated by mean of a Finite Element code in order to complete the experimental observations (Sect. 3). Lastly, the main conclusions are recalled and some prospects are suggested (Sect. 4).

2 Experimental Investigation

2.1 Material and Methods

2.1.1 Limestone Porous Samples

The selected material is a limestone known as 'Lixhe limestone' and extracted from the C.B.R. quarry in Hallembaye (near to Liège, Belgium). It is already well known from the mechanical and hydraulical point of view (Collin et al. 2002; Schroeder 2002; Zaman et al. 1995; Hettema et al. 2002), because its pertains to the same formation as the Ekofisk oil reservoir in the North Sea. It is a very homogeneous rock, made by more than 98 % of calcite, and globally isotropic. Its intrinsic permeability ranges between 10^{-15} and 10^{-16} m^2 and its porosity between 42 and 44 %. To better characterize the internal structure, we performed a porosimetry test by mercury intrusion on three samples. The pore size distribution obtained is presented in Fig. 2, where it appears that the pore diameter is quite homogeneous around the value of 0.6 μm.

Cylindrical samples with a diameter of 18 mm (this size is large enough with respect to the representative length of the micro-structure, 0.6 μm) and variable heights were drilled at the lab. They are first saturated by being soaked into a solution at equilibrium with the material to prevent any dissolution (the solution is obtained by a mixture of water and limestone powder). After 3–4 days and the use of a vacuum pump for a few hours to complete the process, a saturation degree of about 90 % is obtained for all samples. To simplify the analysis of the drying kinetics, we chose to impose a globally unidirectional direction of the water transfer. Samples are thus covered by latex membranes, such as the bottom and the lateral surfaces of the cylinders are hermetically wrapped and a single surface stays available for evaporation (Fig. 3).
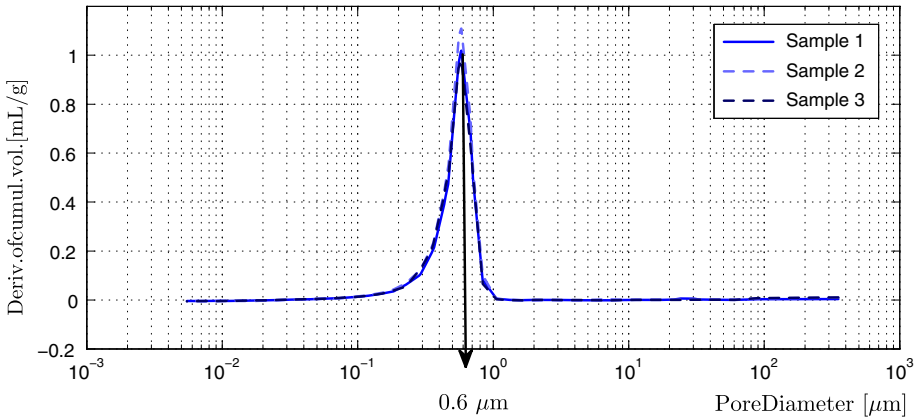
Fig. 2 Pore size distribution in the 3 limestone samples (results obtained by mercury intrusion porosimetry)

Fig. 3 Globally unidirectional water transfer forced within the samples
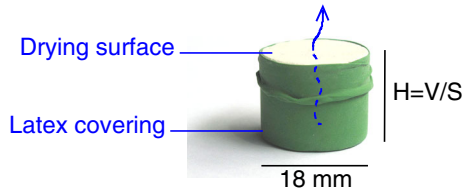
2.1.2 Microdrying Set-up

Drying tests are performed by mean of a convective microdryer, specially designed to dry small individual samples of a few grams. The scheme of this tool is presented in Fig. 4 and, if needed, more details about it can be found in Léonard et al. (2002). One part of the system makes possible to control the air flow velocity thanks to a pneumatic valve connected to a mass flowmeter (no 1 to 4 in Fig. 4a). The other part is able to heat the air up to the chosen temperature with a regulated heat tube (no 5 and 6) but without any control of humidity. Air flows into a drying chamber having a 4×4 cm section (no 9) where temperature and relative humidity are measured (no 7). The sample to study is put in this cell on a supporting grid underneath to a precision weighting device (precision of about 1 mg) connected to a PC to record regular measures of mass (no 8).

Realistic external conditions are the most relevant to apply here since they concern most of the geomaterials in civil engineering. An air flow velocity of 0.8 m/s has thus been chosen. In addition, a value of 50 °C has been considered for the air temperature because it was the lowest possible value with the device. The samples are weighted every 30 s, while temperature and relative humidity (which depends on the external conditions and is of about 5 % here) are checked with the same frequency. The cylinders can be placed whether transversally to the drying chamber (the air flow is thus tangential to the drying surface) or longitudinally (the air flow has thus a frontal incidence on the drying surface). In both cases they have an horizontal position so that gravity has negligible effect on the water transfer during the test (Fig. 4b).
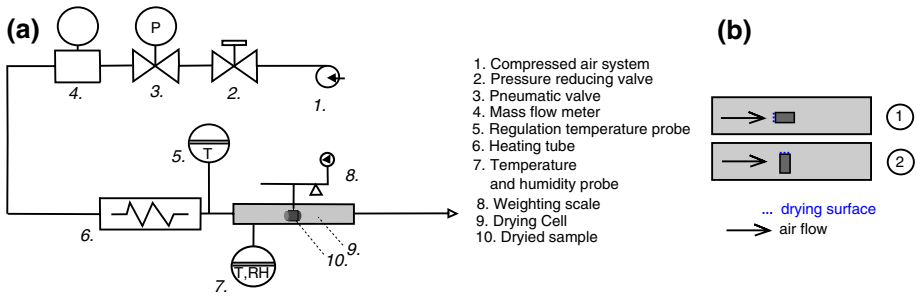
Fig. 4 Microdrying device: global system (**a**), two possible positions of the sample in the drying cell—in an upper view- with frontal incidence of the air flow on the drying surface (case 1) or with a tangential one (case 2) (**b**)

Table 1 Summary of the different configurations tested

	Volume/surface = H (mm)							
	7	10	15	20	25	33	40	50
Nb of tests with frontal air flow	2	1	1	1		1	1	1
Nb of tests with tang. air flow	2		1		1	1		

2.2 Influence of the Sample Volume/Surface Ratio

The first point we decide to investigate is the influence of the geometrical proportions of the sample in order to check:

- if the drying rate during the CRP also depends on this structural parameter,
- if the critical water content W_c varies with it.

To do so, different ratios of volume over drying surface (V/S) have been considered for the samples by only changing the height H of the cylinders. Indeed, since the drying surface is kept constant whatever the height of the samples, the V/S ratio is simply equal to H. The different configurations studied (V/S ranging between 7 and 50 mm) are presented in Table 1. Because the influence of the air flow incidence on the drying surface is not known, both tangential and frontal flows have been considered by changing the sample position. Due to the width of the drying cell (40 mm), higher length than 33 mm is not possible for the transversal position of the cylinder (which corresponds to a tangential air flow) (see Fig. 4b). Finally, the case with $H = 7$ mm has been repeated twice because of poor stability observed for this narrow surface of contact with the support.
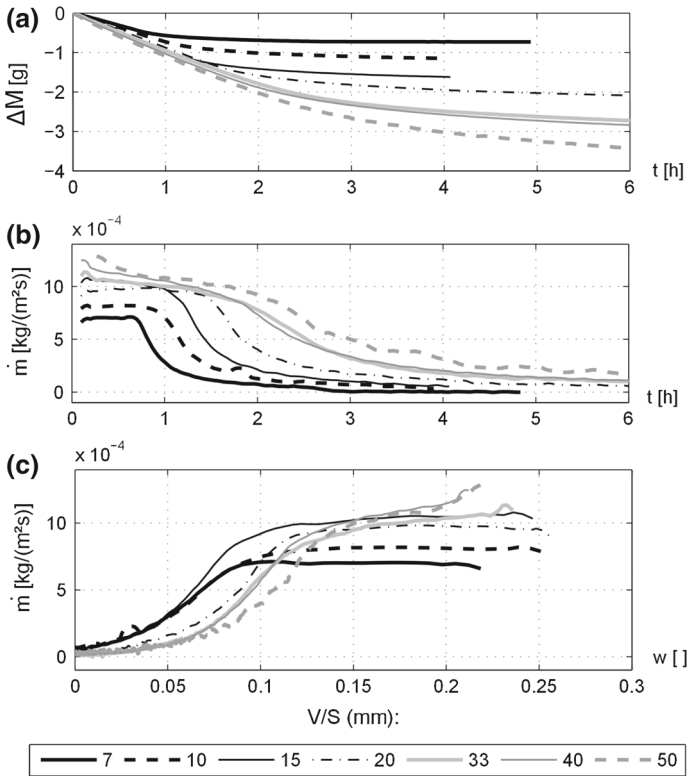
2.2.1 Drying Curves

For each sample, three curves have been plotted: the loss of mass ΔM along time, the evolution with time of the water mass flux $\dot{m}$ across the drying surface S and Krischer's curve, that is to say this same flux but in function of the water content (in kg/kg). $\dot{m}$ is computed as :

$$\dot{m} = \frac{1}{S}\frac{dM}{dt} \qquad (1)$$

Due to the frequency of the mass measures and the limited precision of the weighting scale, this flux undergoes many irregularities. It has thus been processed with a Lanczos filter

Fig. 5 Drying curves for a frontal incidence of the air flow

(Lanczos 1956), in order to be smoother. According to this processing, the derivative of the mass M at a given time t not only considers two data points but a range of measures before and after t. This chosen range, called "semi length filter", can be defined as a number of data points or as a time interval. In the present case a semi-length filter of 90 s was considered.

The drying curves for the seven cases defined for the frontal incidence of the flow are gathered in Fig. 5. We chose to only present the results for this air flow direction which has provided a more complete range of V/S ratios.

Various observations can be made from the three graphs where the CRP and the FRP can be clearly distinguished for the 7 cases.

Firstly, it can be observed from Fig. 5a and b that from H ranging between 7 and about 20 mm, flux and duration of the CRP increase with the height. It means that the longer is the sample, the higher is the volume of water evaporated during the CRP. On the contrary, for H higher than 30 mm this influence is not any more visible: the flux reaches a limit of about 11 kg/m^2/s and a duration of about 1.8 h. It means that, whatever the sample length beyond 30 mm, the volume of water evaporated during the CRP is the same. The water that initially lays deeper than 30 mm from the drying surface cannot thus join the surface in this period, which is very likely due to too high internal limitations for such a distance. These limitations can be detected by the fact that, for the three samples higher than 30 mm, the flux during the CRP is not exactly constant but slightly decreases in the same time as W. As it is commonly considered that during the CRP the water is mainly transferred to the drying surface under

a liquid form, the previous observations remind the concept of a hydraulic connection layer linking the sample surface to an internal desaturation front. As detailed in introduction, such a model has already been proposed to explain the fast water transfer during the first stage of the drying, notably by Lehmann et al. (2008) for which the end of the CRP corresponds to the break of the hydraulic connection.

Secondly, Krischer's curve does not show a clear relation between the critical water content W_c at the end of the CRP and H. However, it can be noticed that between the case with the shortest sample and the case with the longest sample, W_c has slightly increased from 0.08 to 0.14 kg/kg.

2.2.2 Transfer Coefficients

In order to get a better overview of the previous results, mass and heat transfer coefficients have been calculated. To do so, the commonly used limit layer model was considered at the material surface (see Fig. 6). It states that all the transfers from the sample surface toward outside take place by diffusion in a thin layer of thickness δ.

Water mass flux (denoted $\dot{m}$) is proportional to the mass transfer coefficient h_m and is driven by a water content potential, which can be expressed as a concentration difference, an absolute humidity difference, a vapour density difference, etc. We chose to work with a vapour density difference between the material surface and the environment as proposed by Ben Nasrallah and Perre (1988). Heat flux from the environment to the material (denoted $\dot{q}$), is the sum of two terms. One is proportional to the heat transfer coefficient h and is driven by a temperature difference, and one corresponds to the latent heat, directly correlated to the evaporated water mass. The two fluxes are thus expressed as follows:

$$\begin{cases} \dot{m} = h_m(\rho_{v,\text{surf}} - \rho_{v,\text{air}}) & (\text{kg/m}^2/\text{s}) \\ \dot{q} = h(T_{\text{air}} - T_{\text{surf}}) - L\dot{m} & (\text{W/m}^2), \end{cases} \qquad (2)$$

with $\rho_{v,\text{surf}}$ and $\rho_{v,\text{air}}$ being respectively the vapour density at the surface of the porous material and in the surrounding air, T_{surf} and T_{air} being the temperature (in °K) on the surface and in the air, and L being the latent heat of water. h_m and h take into account both the diffusion properties and the thickness of the limit layer.

During the CRP, it is commonly admitted that air in direct contact with the surface is saturated in vapour, and that its temperature is equal to the wet bulb temperature, denoted T_h. In consequence of this vapour saturation, it is considered that no heat is transferred to the sample but that it is all consumed to evaporate the water. h_m and h can thus be obtained as follows:

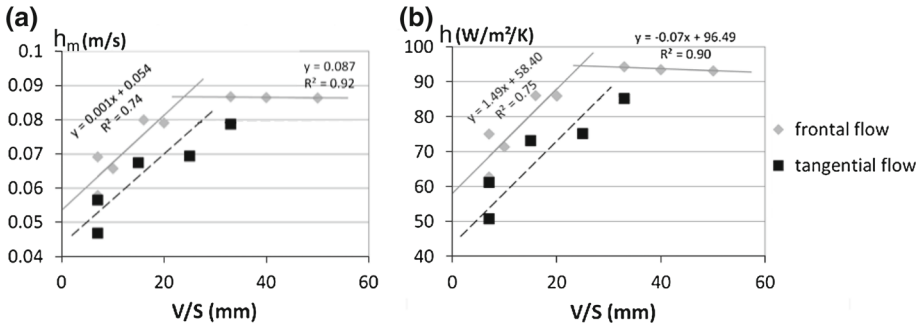**Fig. 6** Limit layer model for the transfers at the sample surface
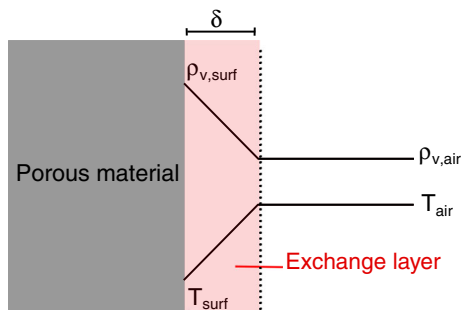
**Fig. 7** Water (**a**) and heat (**b**) transfer coefficients according to the V/S ratio and to the air flow incidence

$$\begin{cases} h_m = \dfrac{\dot{m}_{\text{cst}}}{\rho_{v,\text{sat}} - \rho_{v,\text{air}}} \\ h = \dfrac{L\dot{m}_{\text{cst}}}{T_{\text{air}} - T_h}, \end{cases} \tag{3}$$

with $\dot{m}_{\text{cst}}$ the constant water flux obtained during the CRP and $\rho_{v,\text{sat}}$ the saturated vapour density.

The wet bulb temperature T_h can be iteratively calculated thanks to the relation proposed in Nadeau and Puigalli (1995) which links T_h, the ambient vapour pressure $p_{v,\text{air}}$, the saturated vapour pressure $p_{v,\text{sat}}$ and T_{air}. $p_{v,\text{sat}}$ can be determined thanks to Garrel&Christ empirical expression (Garrels et al. 1965) for temperature between 273 and 303 °K and $p_{v,air}$ thanks to the relative humidity RH of the environment given that: $p_{v,\text{air}} = RH.p_{v,\text{sat}}$. Finally, the densities are deduced from the partial pressures thanks to the ideal gaz law. h_m and h are thus computed for the 13 tests and the results are gathered in Fig. 7 which illustrates the variation of the coefficients with both V/S ratio and the orientation of the air flow.

This figure clearly puts in evidence that h_m and h are not constant as it is commonly considered for a given material submitted to given drying conditions. Indeed, as the drying rate, their values increase with V/S ratio until a given threshold value that corresponds, for the frontal air flow, to a value of V/S between 20 and 30 mm. For the tangential flow, the tendency seems to be the same. However, as no data is available beyond a height of 33 mm (because of the width of the drying chamber), no threshold value is highlighted. In addition to these observations, it seems that aerodynamics has also a consequence on the drying kinetics. A frontal incidence of the air flow induces a higher drying rate during the CRP of about 10 %, probably because, on one hand, it may modify the thickness of the limit layer (see Fig. 6) and, on the other hand, because this limit layer model may not be valid anymore for a highly turbulent flow. The incidence of the flow can also modify the repartition of the relative humidity at the surface of the sample, which has been considered here, in a first approximation, as homogeneous. Finally, these coefficients can be compared to other values found in literature. $h_m = 0.04$ m/s can be found in Gerard (2011) for silt, and values of 0.014 and 0.02 m/s are given by Ben Nasrallah and Perre (1988) for clay brick and wood respectively. Similarly, these authors give $h = 50$, 15 and 23 W/m²/°K for these three materials respectively. These coefficients have been determined for temperature equal or higher than 50 °C. It means that h and h_m are quite high for limestone, and thus that the transfers are relatively fast.

Fig. 8 Water repartition during
the drying of 2 capillary tubes
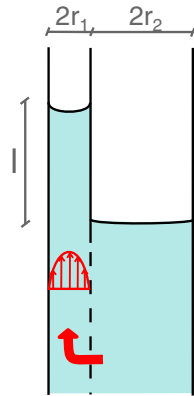
2.2.3 Comparison of the Limit Width of the Hydraulic Connection Layer with Lehmann's Characteristic Length (2008)

According to Lehmann et al. (2008) who studied the hydraulic connection layer during sand drying, the maximum length along which water can flow beyond the saturated front is determined by gravitational, capillary and viscous effects. These effects depending on both the material poro-structure and the external conditions of drying, Lemhann et al. proposed, based on theoretical expressions of the different driving mechanisms, expressions of this maximum length that they called 'characteristic length'. This paragraph aims to compare the limit value we obtained (between 20 and 30 mm) with this theoretical distance.

To express the characteristic length for any porous material, Lehmann et al. base their demonstration on the water transfer within two capillary tubes of radius r_1 and r_2, as presented in Fig. 8. In this simplified model, the characteristic length corresponds to the maximum length l between the water levels in the two tubes. Disregarding gravity, to approach our case in which the samples lay horizontally, the distance of equilibrium between the two levels of water is obtained for balanced effects of capillarity, which enhances the displacement of water in the tubes and viscosity, which limits the displacement of the water in the tubes.

The capillary effects induce a head difference ΔH_{cap} between the two tubes which is expressed as follows (a nil contact angle is assumed between the water and the tubes):

$$\Delta H_{\text{cap}} = \frac{2\sigma}{\rho_w g} \left(\frac{1}{r_1} - \frac{1}{r_2}, \right) \tag{4}$$

with σ the surface tension of water, ρ_w the water density and g the gravity acceleration. Let us now compute the head loss due to viscous dissipation. Writing $\dot{v}_o$ the volumetric flux of evaporation from the whole surface of the system (in m/s) and $\dot{v}$ the hydraulic flux through the fine capillary, it comes by conservation that:

$$\dot{v} r_1^2 = \dot{v}_o (r_1^2 + r_2^2) \tag{5}$$

Lemhann et al. expressed in details the flux $\dot{v}$ according to the Hagen–Poiseuille law, the hydraulic conductivity with respect to r_1, r_2 and the dynamic viscosity η before achieving the expression of the viscous head loss ΔH_v. The same expression of ΔH_v can be obtained by simply writing that the evaporation flux from the whole surface equals the velocity of the

water in the system, expressed with Darcy's law:

$$\dot{v}_o = K \frac{|\Delta H_v|}{l},$$ (6)

with K the hydraulic conductivity which depends on the saturation state and l the length crossed by the water, which corresponds to the length we are looking for.

By equalling ΔH_{cap} and ΔH_v we finally get:

$$l = \frac{K}{\dot{v}_o} \Delta H_{\text{cap}} = \frac{K}{\dot{v}_o} \frac{2\sigma}{\rho_w g} \left(\frac{1}{r_1} - \frac{1}{r_2} \right)$$ (7)

Lemhann et al. proposed to determine ΔH_{cap} by linearising the decrease of saturation degree in the water retention curve, which presents the saturation degree Sr in function of the capillary pressure p_c or in function of the capillary head H_{cap}. We did so as presented in Fig. 12, and obtained $\Delta p_c \approx 3 \times 10^5$ Pa which gives $\Delta H_{\text{cap}} \approx 30$ m. Besides, a mean volumetric water flux of 9×10^{-7} m/s during the CRP can be deduced from Fig. 5. Considering a degree of saturation of the surface varying between 90 and 50 % (the water content is approximatively divided by two at the end of the CRP according to Fig. 5), a saturated hydraulic conductivity equal to 5×10^{-9} m/s gives values of hydraulic conductivity between 3×10^{-9} and 5×10^{-10} m/s for this unsaturated range (using Van Genuchten model of relative permeability whose parameters are justified in Sect. 3). It results a characteristic length l ranging between 1.7 and 10 cm which well fits with our results. However, it must be pointed out that only an order of magnitude can be obtained with Lehmann's formula, given the uncertainty on the relative hydraulic conductivity.

In conclusion, this first campaign highlighted that:

- a hydraulic connection layer may exist during the CRP of this natural rock, as suggested by previous studies for systems where capillary effects are significant,
- this hydraulic connection layer appears to have a limited width of about 20–30 mm. This threshold is probably linked to the material porous structure that restricts the amount of water dried during the CRP. Notably, this value is consistent with the order of magnitude of l proposed by Lehmann et al. (2008) by considering viscous and capillary effects.
- W_c does not seem to be an intrinsic value for the present material with fixed drying conditions since it slightly depends on the sample geometry.

In order to confirm the existence of the hydraulic connection layer and better characterize the water transfers, we then investigated the water repartition within the samples, by mean of an X-ray tomography analysis during the drying test.

2.3 Evolution of the Saturation Profile

2.3.1 X-Ray Microtomography

Tomography has been proved to be very powerful to get information about the drying process, as it makes possible to study in a non destructive, fast and accurate way the internal organization of a given sample. Among various existing techniques, an early use of Nuclear Magnetic Resonance by various authors has to be mentioned. For instance, Pel et al. (1996), McDonald et al. (1996) determined, by assuming diffusion as the only cause of water transfer, apparent diffusion coefficients in function of the water content obtained along profiles during the drying. X-ray tomography imaging, that we use in this study, seems to have been later applied for investigations on drying. We can quote for example the work of Léonard et al.

(2002, 2004), who make appear the constant drying flux by considering the material surface decrease, and links the development of internal limitations for the transfer to crack formation. This last effect is assumed to be due to the moisture gradients induced within the material. Another study led by X-ray tomography concerns the water repartition during the drying of sand columns (Shokri et al. 2009). These authors put in evidence a capillary flow below the evaporation surface, and this high evaporation rate in the first phase of drying could only be explained by liquid flows rather than vapour diffusion.

X-ray tomography imaging lays on the fact that each matter has a specific response to X-ray radiation. The fraction of X-rays that is absorbed or scattered per unit thickness of the material is called "attenuation coefficient" and is denoted μ (in m^{-1}). μ depends on the atomic number (Z) of the matter crossed, the electron density (ρ) and the photon energy (E). A relation was for example proposed by Vinegar and Wellington (1987):

$$\mu = \rho \left(a + \frac{bZ^{3.8}}{E^{3.2}} \right),$$ (8)

where a is called the Klein-Nishina coefficient (it is a function of E), and b is a constant, determined empirically to be equal to 9.8×10^{-24} according to Vinegar and Wellington (1987). The first term of this sum stands for inelastic scattering of the rays by the matter and the second one for photoelectric absorption.

The object studied is submitted to an X-ray source with different radiation angles, each one giving a projection of the attenuation coefficients resulting from of all the points crossed by the rays. In a second stage, reconstruction techniques make possible to have access of the attenuation coefficient of each internal point and to design cross section of the sample.

The X-ray tomographic device used in this study is a Skyscan-1172 X-ray scanner (Skyscan, Belgium). The sample lays on a support that can be rotated in a horizontal plane in order to get the different projections necessary for the reconstruction. The study aims to analyse the water repartition during the drying test, considering the same ambient conditions as previously and the sample with $H = 15$ mm. As the sample has to be removed from the drying chamber to be put in the tomographic device, relevant times are chosen to interrupt the test, given that the CRP lasts approximately 60 min. These times are: 30 min after the beginning of the drying, 60, 90 and 120 min. Two additional scans are considered: one in the saturated state and one after complete drying (the sample is steamed at 105 °C). During the scan, which lasts approximately 15 min, the latex covering is completely closed upon the drying surface to totally stop the drying process. The sample is also weighted with a precision scale (1 mg of resolution) before and after the scan to check that no significant desaturation has occurred. It resulted that, for each scan, no more than 0.01 g of mass was lost. A resolution of 16 μm is chosen for the scan, with an angle of rotation of 0.5° between two projections. The whole sample is analysed, and in total 971 circular cross sections have been recorded along the height H (one section each 16 μm).

2.3.2 Result Process

Two cross sections obtained after reconstruction are presented in Fig. 9. The grey level in this representation is proportional to the attenuation coefficient. In other words, assuming that the density is the only cause of attenuation variation (because of the desaturation), the darker the image is, the denser the material, and thus the more saturated it is. In this figure, the comparison of an almost dry cross section (a) and a very saturated one (b) makes appear that no clear evolution is visible without post-processing the results.
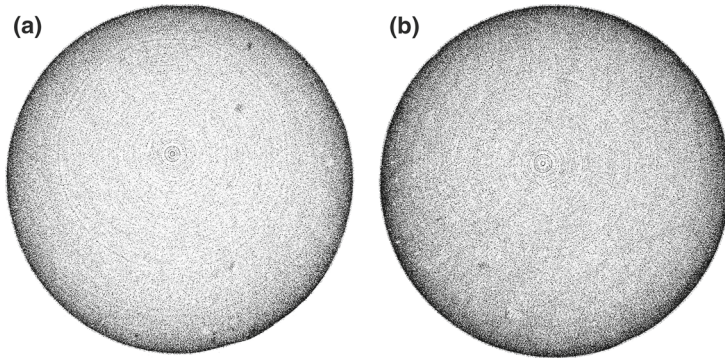
Fig. 9 Cross sections scanned: after 120 min and at 2 mm from the drying surface (**a**), after 30 min and in the deepest part of the sample, 14 mm from the drying surface (**b**) (diameter is 18 mm)

As the water transfer is supposed to be globally unidirectional (at least we are interested only in one direction of transfer), the idea is to determine a global grey level for each cross section to have a numeric scale to quantify the water repartition.

Furthermore, one has to notice that the dark surrounding zone observed in the cross sections, like in Fig. 9, does not correspond to a material or to a water content heterogeneity, but is due to a classical artefact effect in tomography, called 'beam-hardening effect'. Indeed as the radiation source is not monochromatic, the more the distance travelled through the sample is, the more energetic the radiation results (lowest energy waves are absorbed). As the attenuation coefficient μ does not only depend on the density (and the atomic number) but also on the radiation energy E (see Eq. 8), if this last increases for a given material, μ accordingly decreases. In order to minimize this artefact, a ring of around 1.5 mm width around the cross section boundary has been disregarded in the processing. The mean grey level on all the remaining pixels has been computed in each section. This value is normalized to range between 1 for black pixel (maximum density) and 0 for white pixel (minimum density). This quantity has thus no unity.

2.3.3 Density Profile Evolution

The results obtained are exposed in Fig. 10a. In this graph each point corresponds to the normalized grey level of a section at a given time of the drying. The "position" in abscissa locates the section according to its depth under the drying surface. The position of 0 mm thus corresponds to the drying surface and the position of 15 mm to the bottom of the sample. For the drying test considered here (led with the 15 mm height sample), this graph thus illustrates the evolution of the density profile along time. In this graph it appears first a global tendency of the grey level to be lower at the drying surface and at the bottom. Besides, the curves exhibit local heterogeneities as at position of 3, 7.5, 9, 10.5 mm (etc.) where denser levels are visible. Because these 2 density variations can be seen on all curves, including for the totally dry state, it can be deduced that they characterize the solid skeleton, independently from the water content. Therefore, to better follow the water content evolution, the profile standing for the solid skeleton density (with a totally dry state) has been rested to all the profiles. A new profile for 30 min is thus obtained by making the difference between the profile of 30 min of Fig. 10a and the dry profile, a new profile for 60 min obtained by making the difference between the profile of 60 min of Fig. 10a and the dry profile, etc. This second plot is presented

Normalized grey level

Normalized grey level (of water content)
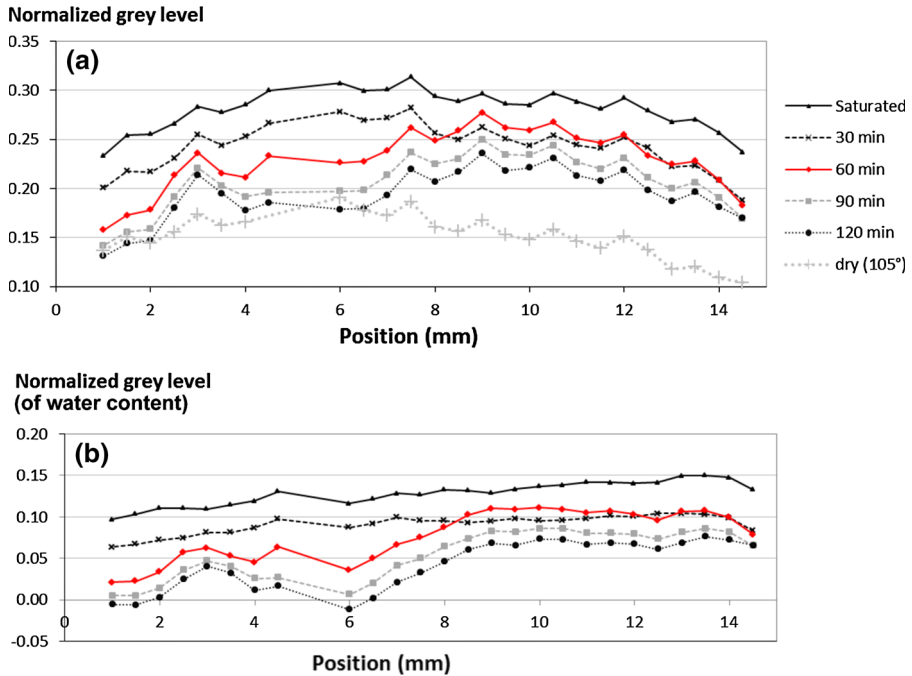
Fig. 10 Evolution of the global density in the sample longitudinal profile (**a**), evolution of the water density in the longitudinal profile (**b**)

in Fig. 10b. By this way, as the original profiles stand for the cumulated density of both the dry porous structure and the water content, the resulting profiles correspond to the density of the porous water only (directly linked to the water saturation degree).

In this new graph, the previous variations have disappeared which makes possible to clearly distinguish two phases concerning the water repartition. In a first period (up to at least 30 min) the initial profile and the profile for 30 min are almost parallel which means that the sample is desaturated as much in its surface as in its deepest part. As the water content is quite homogeneous at the beginning, the saturation remains approximately constant in this stage (by assuming a linear regression between the curves, in Fig. 10a, of the initial saturation degree and the final one −90 to 0 %- it appears that the saturation degree could be around 60 % at 30 min). In a last period (between 60 min up to the end), the curves are also parallel between each others which means a new homogeneous desaturation. However, between 30 and 60 min of test, one can observe significant variations of the water repartition: the water content becomes very low in a top layer (up to 6 mm), a wetted front is visible between 6 and 8 mm while, in the deepest part of the sample (far from 8 mm), the water content does not evolve and is even similar to the 30 min profile. It means that, between 30 and 60 min, the repartition of water is drastically changed with an heterogeneous desaturation: the surface layer is quickly dried while the deep part has kept the same content of water. By relating this phenomenon to the drying curves in Fig. 5, it appears that this transition phase corresponds to the end of the CRP which was observed a little before one hour of test (at around 50 min).

The homogeneous desaturation along the sample in the first period (before 30 min) confirms the assumption of a hydraulic connection layer during the CRP phase which, for this dimension ($H = 15$ mm), is established through the whole the sample height. Such a homo-

geneous desaturation has already be observed in saturation profiles, for example by Pel et al. (1996) who used a scanning neutron radiography to analyse other kinds of geomaterials.

Then, joint analysis of drying curves and cross sections obtained by microtomography appears to be a good way to characterize water transfers in rigid porous media, even if some questions still remain open. First, what are the transfer mechanisms that correspond to the kinetics of such a drying test? What is the limiting phenomenon which explains the end of the CRP and of the hydraulic connection layer? To try to answer these questions, a numerical analysis is proposed in the last part of this study, based on a finite element modelling.

3 Finite Element Simulations

3.1 Finite Element Model

3.1.1 Presentation of the Problem

According to the latest developments in drying modelling, we decided to use an hydro-thermally coupled finite element code (Lagamine, developed at Liege University) to simulate the previous experiment, still focusing on the 15 mm high sample. Mechanical response is disregarded given the absence of noticeable shrinkage and cracking during drying tests. Nodal unknowns of the finite element problem are thus, at each time t, the temperature T^t and the water pressure p_w^t. Balance equations that are solved for this problem are the heat conservation, the mass conservation of water and Kelvin equilibrium between liquid water pressure and relative humidity RH expressed as follows:

$$RH = \frac{\rho_v}{\rho_{v,\text{sat}}} = \exp\left(\frac{(p_w - p_{\text{atm}})M_v}{RT\rho_w}\right), \tag{9}$$

with M_v the molar mass of water, and R the universal gaz constant.

As a first approach, a single-phase flow is considered in the porous medium, with the fluid being the water. This hypothesis means that a constant gas pressure equal to p_{atm} is considered in all the porous medium. Nonetheless, the density of water vapour into the gas is computed thanks to Kelvin relation and makes possible to estimate the fluxes of diffused water vapour.

The constitutive equations are the following.

– At time t, the mass flux of liquid water $\dot{m}_l^t$ is given by Darcy's law (Eq. 10)

$$\dot{m}_l^t = -\rho_w^t \frac{\kappa k_{r,w}}{\eta}\left(\nabla p_w^t + \rho_w^t \boldsymbol{g}\right), \tag{10}$$

with ρ_w the water density, κ the intrinsic permeability, $k_{r,w}$ the relative permeability coefficient, η the dynamic viscosity of water and $\boldsymbol{g}$ the gravity vector.

– For the water vapour, the mass flux $\dot{m}_v^t$ is given by Fick's diffusion law (Eq. 11)

$$\dot{m}_v^t = -D\tau\phi^t(1 - Sr^t)\nabla\rho_v^t, \tag{11}$$

with D the diffusion coefficient of vapour into dry air, τ the tortuosity, Sr the water saturation degree ρ_v the vapour density and ϕ the porosity. As stated above, the water vapour density is obtained by Kelvin equilibrium. According to Philip and De Vries (1957), D is linked to the temperature T and the gaz pressure p_g with the following expression:

$$D = 5.893 \times 10^{-6} \frac{T^{2.3}}{p_g} \tag{12}$$

– For the heat, the flux $\dot{\boldsymbol{q}}^t$ at time t follows conduction, convection and evaporation mechanisms:

$$\dot{\boldsymbol{q}}^t = -\Gamma^t \nabla T^t + (c_{p,w} \dot{\boldsymbol{m}}_l^t + c_{p,v} \dot{\boldsymbol{m}}_v^t)(T^t - T_0) + L \dot{\boldsymbol{m}}_v^t, \tag{13}$$

with Γ the thermal conductivity of the medium, T_0 the initial temperature of the sample, $c_{p,w}$ the specific heat of liquid water and $c_{p,v}$ the specific heat of water vapour.

3.1.2 Geometry

The geometry and the mesh of the model are presented in Fig. 11a. A two dimensional model with axis-symmetric conditions has been considered given the cylindrical shape. Finer mesh is chosen close to the drying surface to follow the transfers with more accuracy.

3.1.3 Boundary Conditions

Nil heat and water fluxes are considered on the lateral and bottom boundaries. On the drying surface a specific boundary condition, developed by Gerard et al. (2008) is taken into account by mean of interface elements (see Fig. 11b). Considering the limit layer model presented in Fig. 6, adaptive mass and heat fluxes are applied on the nodes of each boundary element ($N1, N2, N3$) according to: the external and surface conditions (defined by hygrometry and temperature) and the transfer coefficients h_m and h. External node $N4$ is used to apply the constant external conditions being, here, 50 °C and a water pressure equivalent to the relative humidity of 5 %.

This boundary condition makes possible to simulate realistic problems of convective drying as can be seen for instance in Pardoen et al. (2014).

3.1.4 Initial State

Initially, all nodes (except the external ones) have a temperature of 17 °C, and a water pressure corresponding to 90 % of water saturation. This relation between p_w and Sr is given by the water retention model (detailed by Eq. 14 in next section).

3.2 Parameters of the Model

All the parameters are gathered in Table 2. Material parameters (density, porosity) have been determined experimentally by mean of a Helium pycnometer test. Tortuosity is assumed to be equal to 0.1 by analogy with Gerard et al. (2010) who performed similar simulations on a material having also a very fine porosity (silt). Water density and dynamic viscosity at ambient conditions, as well as intrinsic conductivity of Lixhe limestone refer to literature review. Air entry pressure, fitting parameter n and residual saturation degree Sr_{res} have been calibrated according to Van Genuchten model for the retention curve (the real one was deduced from the intrusion porosimetry experiment, see Fig. 12). This model defines the following relation between the water saturation degree Sr and the capillary pressure $p_c = p_g - p_w$:

$$Sr = Sr_{res} + (1 - Sr_{res}) \left(1 + \left(\frac{p_c}{p_a} \right)^n \right)^{(1/n-1)}, \tag{14}$$
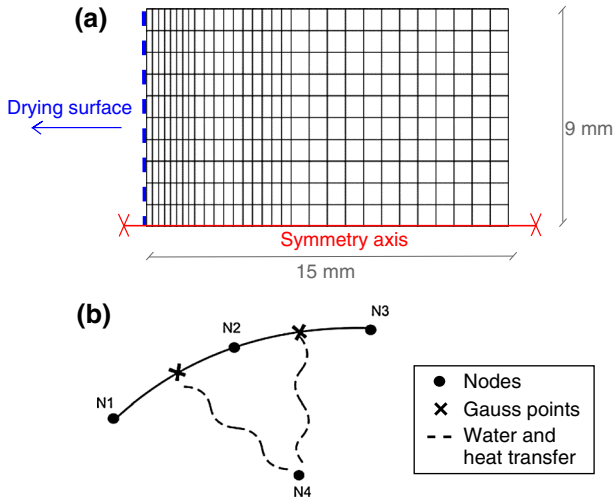
Fig. 11 Geometry, mesh and specific boundary conditions of the model (**a**). Details of the hydro-thermal boundary element for the drying surface (Gerard et al. 2008) (**b**)

where Sr_{res} is the residual saturation degree, n and p_a are two fitting parameters. p_a is usually called air entry pressure.

The relative permeability coefficient also results from the retention parameters of Van Genuchten model:

$$k_{r,w} = \sqrt{Sr} \left(1 - \left(1 - Sr^{1/m}\right)^m\right)^2, \qquad (15)$$

considering that the parameter m is equal to $1-1/n$ ($m = 0.83$ here).

The specific heat of liquid water and water vapour are considered as known datas, as well as the latent heat of water vaporisation. Calcite specific heat is chosen according to Clauser (2011). An homogeneous thermal conductivity is taken over the medium and, because of a lack of datas, it is considered constant whatever the saturation degree. A mean value has been computed thanks to calcite, water and air thermal conductivities which can be found in Clauser and Huenges (1995). Mass and heat transfer coefficients have already been estimated thanks to the drying test for $H = 15$ mm.

### 3.3 Comparison of Numerical Simulations with Experiments

3.3.1 Drying Curves

The first task is to check the numerical results with respect to the experimental ones. With all the parameters of Table 2, the three drying curves obtained are presented in Fig. 13 together with the experimental ones.

First of all, the mass evolution during time (Fig. 13a) is almost superposed with the experimental mass recorded, without processing to any additional calibration (all parameters being determined in advance from experiments or literature). The exact value of CRP water flux (around 10^{-3} kg/m^2/s) is also well captured by the numerical model as shown by the water flux evolution during time (Fig. 13b) and along water content (Fig. 13c). Moreover, the

Table 2 Model parameters

Material parameters			
ρ_s	Solid density	2,710	kg/m^3
ϕ	Porosity	0.4	
τ	Tortuosity	0.1	
Hydraulical parameters			
ρ_w	Liquid water density	1,000	kg/m^3
η	Water dynamic viscosity	1E−3	Pa.s
κ	Intrinsic permeability	5E−16	m^2
p_a	Air entry pressure	6.5E5	Pa
n	VG fitting parameter	5.85	
Sr_{res}	Residual water saturation degree	0.035	
Thermal parameters			
$c_{p,w}$	Liquid water specific heat	4,180	J/kg/K
$c_{p,v}$	Water vapour specific heat	1,000	J/kg/K
$c_{p,s}$	Solid specific heat	1,780	J/kg/K
Γ	Medium thermal conductivity	0.9	W/m/K
L	Water vaporisation latent heat	2.5E6	J/kg
Transfer parameters			
h_m	Mass transfer coefficient	0.076	m/s
h	Heat transfer coefficient	82.9	W/m^2/K
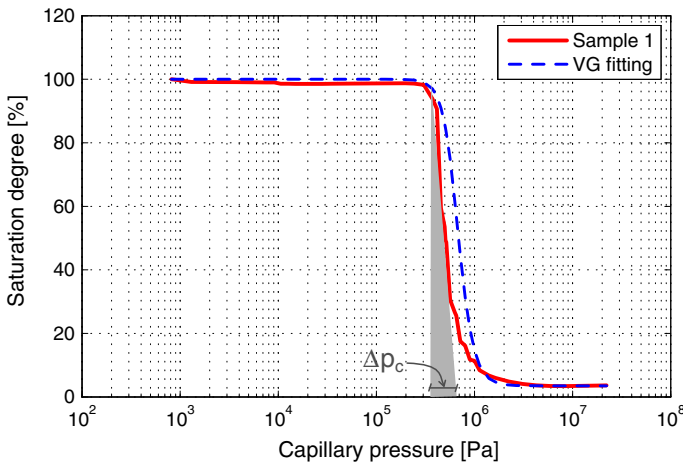
Fig. 12 Calibration of Van Genuchten ('VG') water retention model, thanks to the first intrusion porosimetry test presented in Fig. 2

end of CRP is consistently reached after around 50 min and for a water content approaching 0.12 kg/kg.

However, one can notice a discrepancy between the experimental and the numerical flux curves, just before reaching the dry state. Indeed, numerical results exhibit a sudden transition:
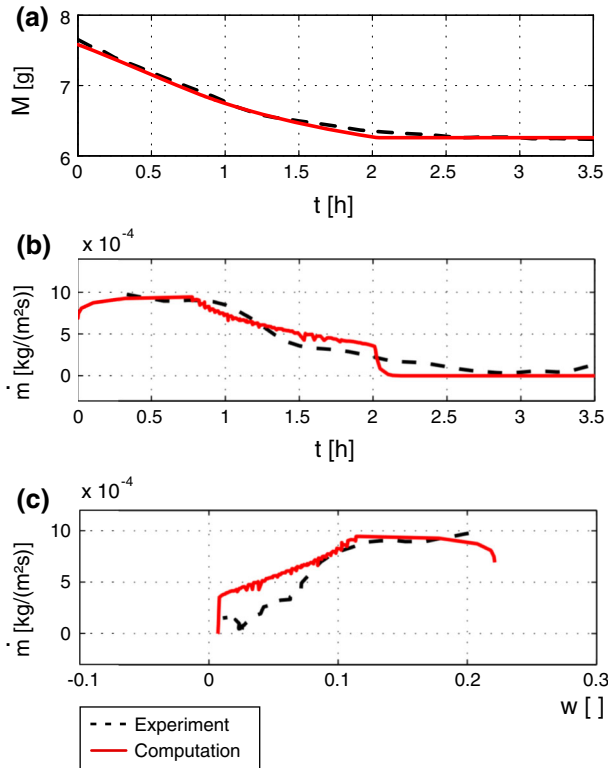
Fig. 13 Comparison of the computation results with the experimental ones for $H = 15$ mm

the flux suddenly falls after 120 min (Fig. 13b) once the residual water content is obtained (see Fig. 13c). Such a discontinuity is not observed experimentally.

3.3.2 Water Content Profile

The evolution of the saturation profile along the sample has also been extracted and is plotted in Fig. 14a. Comparing these profiles to the experimental ones (Fig. 10b) confirms that the desaturation of the sample is quite homogeneous along the depth during the first 30 min of the test. A dry layer at the top of the sample appears after 50 min, as the same time as the end of CRP observed in both numerical and experimental drying curves.

As numerical analysis makes possible to get more datas than experiments, the water content evolution around the end of the CRP was focused on by mean of many time steps. Compared to the experimental water content profiles, it appears that the transition from an homogeneous desaturation and an heterogeneous desaturation along the sample in not as sudden as it previously seemed. Before the end of the CRP, we can already observe that, from around 30 min, the top of the sample is dried faster than the rest of the sample. It means that internal limitations to the water transfer appear from this time, without directly leading to the end of the CRP (obtained later, at 50 min). It thus makes clearer the competition between internal and external transfers: even for increasing internal limitations, the external evaporation demand still governs the global drying rate until a certain point. The end of the
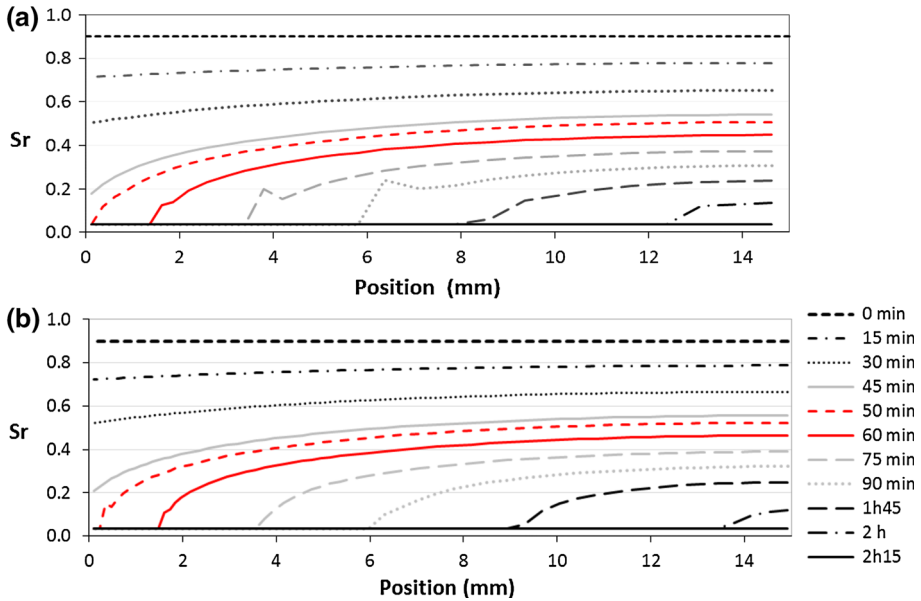
Fig. 14 Evolution of the profiles of water saturation degree: with coarse mesh (**a**) with fine mesh (**b**)

CRP is not explained by a single phenomenon but by the transition of the prevailing water transfer mechanism.

Finally, the results of the computation show a receding of the wetted front within the sample, which is consistent with the experimental results until 90 min. Nevertheless, after this time, the receding is faster numerically than experimentally. This means that we may miss one phenomenon in the drying process. More investigations are necessary to understand this point. From 50 min, one can notice that all the curves exhibit a slight discontinuity at the wetted front (for instance at 1.8 mm for 60 min, at 4 mm for 75 min, 6 mm at 90 min, etc.). As this was supposed to be a numerical instability linked to the sharp pattern of the water retention curve, the computation was led with a finer mesh to regularize the results. With twice as many elements in each direction of the model, these irregularities indeed totally disappear (see Fig. 14b), which confirms that they are not physical.

3.4 Water Content of the Surface at the End of CRP

In Fig. 14, we can observed that the CRP ends when the surface elements begin to be completely desaturated (at 50 min). This point can appear questioning, notably with regard to the 'wetted surface model' which states that CRP can be sustained only for a sufficient water content at the sample surface (see introduction).

To try to understand how the constant flux can be sustained until an almost dried state of the surface, we plotted the saturation degree Sr as well as the relative humidity RH in function of the capillary pressure p_c (see Fig. 15). The first relation (between Sr and p_c) comes from the water retention within the porous material while the second one (between p_c and RH) comes from Kelvin equilibrium at the surface of the sample. This graph first shows that the very homogeneous pore size in this limestone leads to a sharp decrease of Sr with p_c. Besides, RH keeps almost constant up to very high values of p_c, corresponding to very
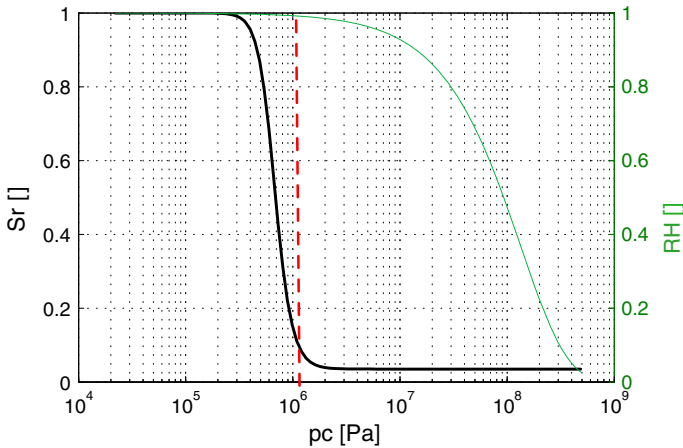
Fig. 15 Justification of the quasi-dry state of the surface sample at the end of CRP

low values of the water saturation degree (such a state corresponds for instance to the dotted line in the graph 15). We have to keep in mind that the drying flux is directly proportional to the relative humidity at the surface, which is the only variable in Eq. 2 (for constant ambient conditions). The constant drying flux thus starts to decrease for an almost dry state of the sample surface.

3.5 Lines of Improvement

Two main differences of the numerical results with respect to the experiments have been pointed: the sudden fall of the flux obtained as soon as the residual saturation degree is obtained (at 120 min), and a too fast recede of the wetted front in the computation from 90 to 120 min. These two points seem to be linked one with another since it is likely that the too high computed drying rate up to 120 min leads to the sudden fall of the evaporation rate. Consequently, it seems relevant to enhance the simulations by increasing the internal limitations that drive the global drying flux from 50 min. We thus performed a parametric analysis on the intrinsic permeability κ. This gave the drying curves presented in Fig. 16.

One can observe that greater values of κ (which corresponds to a decrease of internal limitations) leads to drying curves that exhibit an almost total desaturation during the CRP, with a constant flux along nearly all the test. Furthermore, plotting the saturation profiles for $\kappa = 5 \times 10^{-14}$ m^2 confirms that there is not any more internal limitations to the transfer since the profiles obtained are quasi parallel one to another until the end of the test.

On the contrary, decreasing the intrinsic permeability indeed reduces the discrepancy with experimental results, as seen for $\kappa = 4 \times 10^{-16}$ m^2. Nevertheless, many numerical instabilities are visible for this case, showing the difficulty of convergence of the computation at the end of the CRP (the time step are automatically reduced by the code for a non-convergence, leading to unstable values of the flux). Finally, lower values of κ could not be obtained because of non-convergence. This is probably linked to the sharp pattern of the water retention curve that characterizes the material.

In conclusion, this numerical analysis showed that it is relevant to model the water transfer by mean of simple convective and diffusion laws with Darcy's and Fick's relations. Besides, it made possible to distinguish clearly the apparition of the first internal limitation to the water
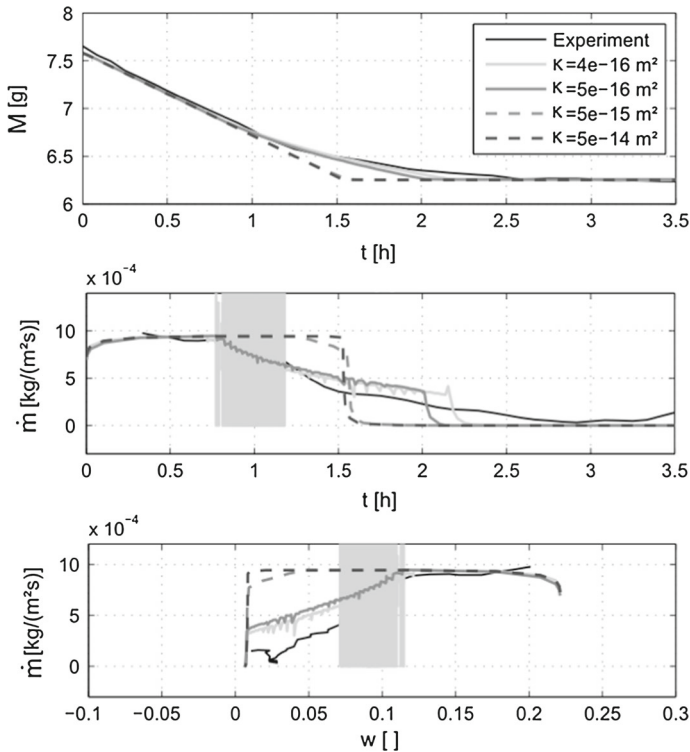
Fig. 16 Influence of intrinsic permeability κ

transfer from the first decrease of the CRP flux. The relation between the surface moisture content and the end of the CRP is shown to be strongly dependant on the material as it is linked to the pore size distribution. Finally, the intrinsic permeability, which cannot always be determined with much precision, plays, as expected, a key role in the FRP modelling. For very impermeable materials, as clays, etc., this value could be calibrated from the numerical results.

4 Conclusion

This study made possible to get a large quantity of information about the drying kinetics by mean of simple and relevant experimental protocols, combining slenderness effect investigation and tomography analysis.

First, it has been highlighted by the two experimental campaigns that, even for a natural porous structure and very fine pores (around 0.6 μm), a hydraulic connection layer characterizes the flux during the CRP. Moreover, the maximum width of this layer could be determined: it achieves 20–30 mm for the chosen ambient conditions. Very interesting is to relate this limit width to the characteristic length proposed by Lemhann et al. (2008). The good agreement between these two dimensions confirms the capillary and viscous effects that drive the hydraulic flows in the unsaturated porous media.

Due to the limited amplitude of this hydraulic connection layer, the critical water content at the end of the CRP is unlikely an intrinsic value, but more probably depends on the sample geometry which was observed, to a certain extent, for the Krischer's curves obtained with the different sample heights.

With the numerical approach, the finite element simulation showed that, at least for this rigid material, a simple hydro-thermal coupling gives very satisfying results, which, furthermore, are predictive since no parameters need to be calibrated a posteriori. Simple Darcy's and Fick's laws, with conduction, convection and evaporation relations for the heat transfer, enable to describe the kinetics.

Finally, the numerical modelling allows to understand more accurately the drying process. The computed evolution of the saturation profiles around the end of the CRP revealed the duration of the competition period between the internal and the external limitations that finally ends in the drying flux decrease.

Concerning rigid porous materials, many points are still to investigate, notably the influence of the drying conditions on the hydraulic connection layer width, the pattern of the capillary flow in this layer, etc. Furthermore, this experimental approach can be considered for many porous materials, notably for non-rigid natural media (as clay for instance) whose shrinkage and cracking are essential features and could be determined by the same tomography tool. Simulating such mechanical response also represents a key numerical aspect.

References

Ben Nasrallah, S., Perre, P.: Detailed study of a model of heat and moass transfer durin convective drying of porous media. Int. J. Heat Mass Transf. **31**(5), 957–967 (1988)

Cariou, S., Skoczylas, F., Dormieux, L.: Experimental measurements and water transfer models for the drying of argillite. Int. J. Rock Mech. Min. Sci. **54**, 56–69 (2012)

Ceaglske, N.H., Hougen, O.: Drying granular solids. Ind. Eng. Chem. **29**(7), 805–813 (1937)

Clauser, C.: Thermal storage and transport properties of rocks, i: heat capacity and latent heat. Carbon **6**(2), 230 (2011)

Clauser, C., Huenges, E.: Thermal conductivity of rocks and minerals. AGU Ref. Shelf **3**, 105–126 (1995)

Collin, F., Cui, Y.J., Schroeder, C., Charlier, R.: Mechanical behaviour of lixhe chalk partly saturated by oil and water: experiment and modelling. Int. J. Numer. Anal. Methods Geomech. **26**(9), 897–924 (2002)

Faure, P., Coussot, P.: Drying of a model soil. Phys. Rev. E **82**(3), 036,303 (2010)

Garrels, R., Christ, C., Solutions, M.: Equilibria, pp. 213–233. Editorial Harper & Row, New York (1965)

Gerard, P.: Impact des transferts de gaz sur le comportement poro-mécanique des matériaux argileux/impact of gas transfers on the poro-mechanical behaviour of argillaceous materials. PhD thesis, Universit de Liège (2011)

Gerard, P., Charlier, R., Chambon, R., Collin, F.: Influence of evaporation and seepage on the convergence of a ventilated cavity. Water Resour. Res. **44**(5), W00C02 (2008)

Gerard, P., Léonard, A., Masekanya, J.P., Charlier, R., Collin, F.: Study of the soil-atmosphere moisture exchanges through convective drying tests in non-isothermal conditions. Int. J. Numer. Anal. Methods Geomech. **34**(12), 1297–1320 (2010)

Hettema, M., Papamichos, E., Schutjens, P.: Subsidence delay: field observations and analysis. Oil Gas Sci. Technol. **57**(5), 443–458 (2002)

Keey, R.B.: Introduction to Industrial Drying Operations. Pergamon press, Oxford (1978)

Ketelaars, A., Pel, L., Coumans, W., Kerkhof, P.: Drying kinetics: a comparison of diffusion coefficients from moisture concentration profiles and drying curves. Chem. Eng. Sci. **50**(7), 1187–1191 (1995)

Krischer, O.: Trocknungstechnik. i. Die wissenschaftlichen Grundlagen der Trocknungstechnik Berlin, G6ttmgen/l feidelberg: Springer (1956)

Lanczos, C.: Applied analysis, 539 pp (1956)

Laurindo, J., Prat, M.: Numerical and experimental network study of evaporation in capillary porous media. Drying rates. Chem. Eng. Sci. **53**(12), 2257–2269 (1998)

Lehmann, P., Assouline, S., Or, D.: Characteristic lengths affecting evaporative drying of porous media. Phys. Rev. E **77**(056), 309 (2008)

Léonard, A., Blacher, S., Marchot, P., Crine, M.: Use of X-ray microtomography to follow the convective heat drying of wastewater sludges. Dry. Technol. **20**(4–5), 1053–1069 (2002)

Léonard, A., Blacher, S., Marchot, P., Pirard, J.P., Crine, M.: Measurement of shrinkage and cracks associated to convective drying of soft materials by X-ray microtomography. Dry. Technol. **22**(7), 1695–1708 (2004)

Léonard, A., Blacher, S., Marchot, P., Pirard, J., Crine, M.: Convective drying of wastewater sludges: influence of air temperature, superficial velocity, and humidity on the kinetics. Dry. Technol. **23**(8), 1667–1679 (2005)

Léonard, A., Blacher, S., Nimmol, C., Devahastin, S.: Effect of far-infrared radiation assisted drying on microstructure of banana slices: an illustrative use of X-ray microtomography in microstructural evaluation of a food product. J. Food Eng. **85**(1), 154–162 (2008)

May, B., Perré, P.: The importance of considering exchange surface area reduction to exhibit a constant drying flux period in foodstuffs. J. Food Eng. **54**(4), 271–282 (2002)

McDonald, P., Pritchard, T., Roberts, S.: Diffusion of water at low saturation levels into sandstone rock plugs measured by broad line magnetic resonance profiling. J. Colloid Interface Sci. **177**(2), 439–445 (1996)

Musielak, G., Banaszak, J.: Non-linear heat and mass transfer during convective drying of kaolin cylinder under non-steady conditions. Transp. Porous Media **66**(1–2), 121–134 (2007)

Nadeau, J., Puigalli, J.: Detailed study of a model of heat and mass transfer during convective drying of porous media. Lavoisier (1995)

Pardoen, B., Levasseur, S., Collin, F.: Using local second gradient model and shear strain localisation to model the excavation damaged zone in unsaturated claystone (in revision). Rock Mech. Rock Eng. (2014)

Pel, L., Brocken, H., Kopinga, K.: Determination of moisture diffusivity in porous media using moisture concentration profiles. Int. J. Heat Mass Trans. **39**(6), 1273–1280 (1996)

Philip, J., De Vries, D.: Moisture movement in porous materials under temperature gradients. Trans. Am. Geophys. Union **38**, 222–232 (1957)

Rousset-Tournier, B., Mazerolle, F., Géraud, Y., Jeannette, D.: Rock drying tests monitored by X-ray computed tomographythe effect of saturation methods on drying behaviour. Geol. Soc. Lond. Spec. Publ. **215**(1), 117–125 (2003)

Schroeder, C.: Du coccolithe au réservoir pétrolier. PhD thesis, University of Liege (2002)

Shaw, T.: Drying as an immiscible displacement process with fluid counterflow. Phys. Rev. Lett. **59**(15), 1671 (1987)

Sherwood, T.: The drying of solids I. Ind. Eng. Chem. **21**(1), 12–16 (1929)

Sherwood, T.: The drying of solids III mechanism of the drying of pulp and paper. Ind. Eng. Chem. **22**(2), 132–136 (1930)

Shokri, N., Lehmann, P., Or, D.: Critical evaluation of enhancement factors for vapor transport through unsaturated porous media. Water Resour. Res. **45**(10), (2009)

Van Brakel, J.: Mass transfer in convective drying. Adv. Dry. **1**, 217–267 (1980)

Vinegar, H.J., Wellington, S.L.: Tomographic imaging of three-phase flow experiments. Rev. Sci. Instrum. **58**(1), 96–107 (1987)

Whitaker, S.: Simultaneous heat, gas and momentum transfer in porous media: a theory of drying. Adv. Heat Trans. **13**, 119–203 (1977)

Yiotis, A., Stubos, A., Boudouvis, A., Tsimpanogiannis, N., Yortsos, Y.: Pore-network modeling of isothermal drying in porous media. Transp. Porous Media **58**(1–2), 63–86 (2005)

Zaman, M.M., Abdulraheem, A., Roegiers, J.C.: Reservoir Compaction and Surface Subsidence in the North Sea Ekofisk Field, vol. 41. Elsevier, Amsterdam (1995)